Research Article Vol. 29, No. 3 / 1 February 2021 / Optics Express 4105
Optics EXPRESS

High sensitivity pressure measurement using optical fibre sensors mounted on a composite diaphragm

LAURA F. J. AIME,[1] THOMAS KISSINGER,[1] STEPHEN W. JAMES,[1,*] EDMON CHEHURA,[1] ALBERTO VERZELETTI,[2] AND RALPH P. TATAM[1]

[1]Centre for Engineering Photonics, Cranfield University, Cranfield, MK43 0AL, UK
[2]Composite R&D, Mercedes, Brackley NN13 7BD, UK
[*]s.w.james@cranfield.ac.uk

Abstract: A pressure sensor specified for aerodynamic applications and based on optical fibre strain sensors mounted on a circular glass fibre reinforced polymer membrane is presented. The use of two fibre optic strain sensing technologies is explored, the novel intrinsic fibre segment interferometry (FSI) approach and fibre Bragg gratings (FBGs), with the use of FSI shown to offer a pressure resolution that is 15 times larger than that achieved using an FBG. A number of design and fabrication issues are considered, including the position of the fibres relative to the neutral axis of the membrane and the influence of the membrane support structure on the thermal and pressure sensitivities of the sensor, with particular regards to pressure and temperature discrimination.

1. Introduction

The understanding of complex flows around aerodynamic structures is of importance in areas ranging from gas turbines to airframes and automobiles. The variables of interest for a basic aerodynamic analysis of a structure are its geometry and the local strain, pressure and temperature. Established approaches include photogrammetry [1] for shape measurement, unsteady piezoresitive sensors such as Kulites for pressure measurement [2,3], resistive foil strain gauges for the measurement of surface strain [4] and thermocouples for surface temperature measurement [5]. There is increasing interest in the use of optical fibres to fulfil these measurement needs [6], as they offer a number of widely accepted benefits, including their small dimensions, light weight, the ability to multiplex arrays of sensors and the potential for embeddment in fibre reinforced polymer structures. The use of intrinsic optical fibre based approaches, where the properties of the modes propagating within the fibre core are perturbed by environmental parameters such as temperature and strain, is well-established across a number of industrial sectors, with the fibre Bragg grating (FBG) being perhaps the approach most widely adopted for multiplexed point sensing [7]. The use of optical fibre based shape sensors on aerodynamic structures has been reported [8].

The ease of the multiplexing of FBG sensors, coupled with the potential for the development of a sensor where the fibre is laid parallel to the surface of the structure, has driven interest in the development of FBG based pressure sensors. However, the inherent sensitivity of intrinsic optical fibres to hydro static pressure is low [9] and so a range of techniques to facilitate pressure sensing using FBGs by transducing the pressure into an axial strain acting on the optical fibre have been reported [10]. These include embedding the fibre in a polymer material [11], the transverse loading of a sub-section of an FBG [10] and mechanical enhancement using a triangular cantilever

#416715 https://doi.org/10.1364/OE.416715
Journal © 2021 Received 4 Dec 2020; revised 15 Jan 2021; accepted 15 Jan 2021; published 25 Jan 2021

Optics EXPRESS

[12], a bubble housing [13] and a piston [14]. The pressure sensitivities exhibited by these approaches are in part limited by the 1 pm resolution of typical Bragg wavelength shift resolution of commercial FBG interrogation systems, and are low for an aerodynamic application targeted for this sensor, which required a measurement range of order 100 kPa and a resolution of order 10 Pa. An alternative approach involves measurement of the strain induced in the membrane by the pressure dependent deflection, which offers the possibility for multiplexing a serial array of fibre optic pressure sensors when, for example, FBGs are used as the strain sensors. A number of materials have been used to form the diaphragm, including rubber [15,16], polymers [17], stainless steel [18,19] and carbon fibre reinforced polymer [20]. Detailed design parameters are reported in Table 1. While rubber offers the highest sensitivity for a given dimension, it exhibits significant hysteresis. Achieving comparable sensitivities would require the use of very thin metal foils, which would not be sufficiently robust and show nonlinear performance. In a previous report [21] we described a pressure sensor exploiting a glass fibre reinforced polymer membrane (GFRP) instrumented with an FBG. The use of GFRP offers flexibility in the selection of membrane properties, and thus pressure measurement performance, primarily through control of membrane thickness, which allowed the design of a sensor that provided a sensitivity of 56.7 pm/kPa over a working range of 0 to 35 kPa, with a resolution of 21 Pa at a bandwidth of 250 Hz using a commercially available FBG interrogator with 1 pm wavelength resolution [21].

Table 1. Pressure sensors using FBGs to measure pressure induced strain in diaphragms

Material	Diameter (mm)	Thickness (mm)	Sensitivity (pm/kPa)	Range (kPa)	Reference
Rubber	5.5	0.6	8.8	0 to 160	[15]
Rubber	7	1	7	100 to 400	[16]
Stainless Steel	30	1.5	1.57	0 to 1000	[18]
Stainless Steel	15 (square)	0.5	0.62	0 to 2000	[19]
Carbon Fibre	57	0.2	18	0 to 98	[20]
Polydimethylsiloxane	50	1.4	1400	0 to 0.1	[17]
Nitrile Rubber	50	1.4	400	0 to 1	[17]
Polyurethane	50	1.4	400	0 to 0.8	[17]

We recently reported a new approach to the demodulation of the signals from an array of intrinsic interferometric fibre optic strain sensors, termed fibre segment interferometry (FSI), that is capable of providing a strain resolution of sub $n\epsilon/\sqrt{Hz}$ [22]. The approach uses a simple and robust optical system comprising a telecommunications distributed feedback (DFB) laser, a fibre optic circulator and a photo-diode to interrogate interferometers formed between an array of in-fibre reflectors using the range resolved interferometry (RRI) technique [23]. In RRI, the sinusoidal modulation of the optical frequency of the output from the DFB laser imposes a path length dependent phase modulation on the interferometers formed between the in-fibre reflectors and a reference reflector, typically the cleaved end face of the optical fibre. This generates a unique carrier signal for each reflector with characteristics determined by the path length imbalance in the corresponding interferometer. Changes in the phase of each interferometer can be determined with high resolution using the RRI approach [23]. A simple subtraction process allows the phase of the segment interferometer formed between any pair of reflectors in the array to be determined, removing any sensitivity to influences beyond the desired fibre segment [22].

In this paper, a pressure sensor based on the measurement of strain in a diaphragm using fibre optic strain sensors is described. The sensor design principles and material choices are discussed, and the performance of the approach when using FSI to measure the diaphragm strain is compared with that of using an FBG, with the FBG and FSI sensors co-located on the

Optics EXPRESS

same membrane. Furthermore, the dependence of the pressure sensitivities on temperature are characterised and future routes to temperature-compensated pressure measurements discussed.

2. Materials and methods

2.1. Sensor principle

The sensor consists of a circular glass fibre reinforced polymer (GFRP) membrane that deflects in response to applied pressure, where the deflection is monitored by the measurement of strain using an optical fibre sensor. The design was based initially on the elastic plate theory of a circular clamped disc, where the equation for a circular clamped plate under uniform pressure, P, is given by [24] :

$$w = \frac{P}{64}\frac{r^4}{D}(1 - \frac{a^2}{r^2})^2 \tag{1}$$

Here w is the deflection at point a along the radius, r, of the plate and D is the flexural rigidity given by:

$$D = \frac{Et^3}{12(1 - v^2)} \tag{2}$$

where E and v are the Young's Modulus and Poisson's ratio of the plate, respectively, and t is its thickness. The radial strain ε can be calculated using the derivative of the deflection [24], which shows that the maximum radial strain appears in the centre of the membrane (3). The strains developed in the optical fibre are calculated for the core position, where light propagates, which is displaced from the surface of the membrane by the radius of the optical fibre (assuming a negligible glue-line thickness) (4).

$$\varepsilon = \frac{t}{2}\frac{1}{r}\frac{\delta w}{\delta r} \tag{3}$$

$$\varepsilon_{OpticalFibre} = \frac{t + d_{opticalfibre}}{2}\frac{1}{r}\frac{\delta w}{\delta r} \tag{4}$$

These equations are applicable only in the small deflection regime, where the deflection is less than 20% of the thickness of the plate, but they may be used to inform the design of the sensor, helping to define the selection of materials and the diameter of the plate given the resolution of the sensor interrogator. In this paper, a sensor previously designed for an automotive application [21] has been further developed. This development employed a GFRP diaphragm with a free diameter of 21.5 mm and a thickness of 0.23 mm, Young's Modulus 26.5 GPa and Poisson ratio of 0.15. Assuming that an optical fibre of diameter of 0.125 mm, corresponding to a SMF 28 optical fibre with its buffer coating removed, was bonded to the surface of the membrane, Eq. (4) predicts a pressure resolution of 23 Pa when the sensor is interrogated using a commercial FBG interrogator of resolution 1 pm.

For the experiments reported here, the diameter of the membrane was increased to 32 mm to enable it to be bonded to the support structure, in this instance made from aluminium, that served as a pressure chamber for characterisation and calibration in the laboratory. The mounting of the membrane was such that an annulus of width 5.25 mm was bonded to the support structure, leaving the 21.5 mm diameter section to deform in response to pressure. An image of the sensor, along with a schematic diagram, is provided in Fig. 1.

Two optical fibres were surface bonded along the diameter of the membrane. One of the fibres contained an FBG of length 4 mm, reflectivity 50% and central wavelength 1542 nm, while the other contained three reflectors, each separated by 10 mm, forming 3 fibre segment interferometers, as shown in Fig. 1 and illustrated in Fig. 2. The FSI reflectors took the form of ultrashort (of length of order 250 microns) and low reflectivity (of order 35 ppm) fibre Bragg gratings (LR FBGs), each having a centre wavelength of 1521 nm and a full-width-half-maximum reflection bandwidth of approximately 5 nm. This ensured that the LR FBG reflector provided

Optics EXPRESS

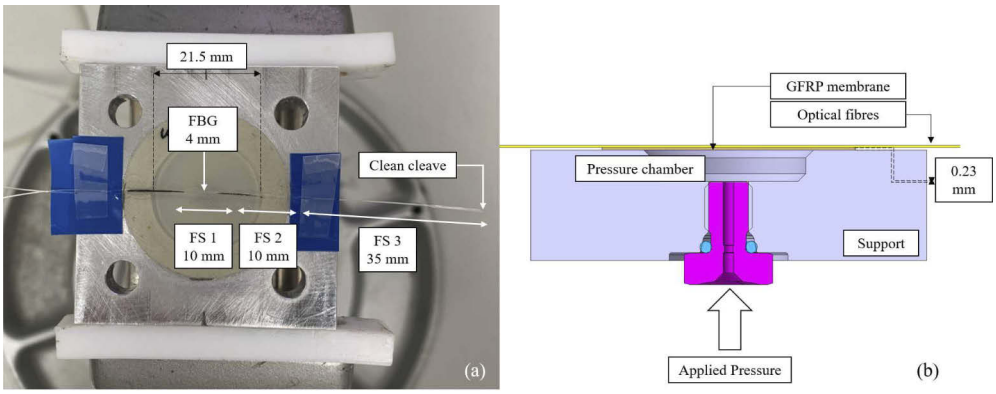

Fig. 1. (a) shows an image of the optical fibre pressure sensor, comprising a GFRP membrane instrumented with two optical fibres, one containing an FBG and the other one containing 3 fibre segment interferometers (FS 1, FS 2 and, FS 3) mounted within an aluminium support structure. (b) shows a schematic of the sensor with the pressure chamber on one side of the membrane and ambient pressure on the other.

a reflected signal at the wavelength of the laser used in the FSI interrogator, irrespective of the wavelength shift caused by the deflection of the membrane or changes in temperature. The locations of the fibre segment interferometers, denoted as FS 1, FS 2 and, FS 3, are shown in Fig. 2, while the sensor parameters are summarised in Table 2.

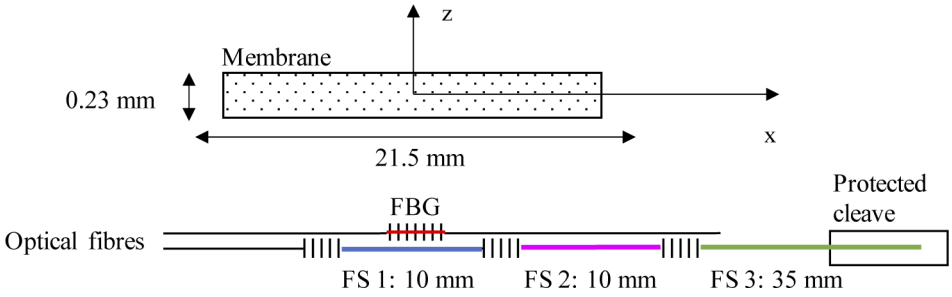

Fig. 2. Schematic of the two optical fibres, one containing an FBG and the other one containing 3 fibre segment interferometers (FS 1, FS 2 and, FS 3) and their positions on the membrane. Not to scale.

Table 2. Optical fibre sensor properties. All lengths measured to an uncertainty of ± 0.1 mm

	FBG	FSI
Grating length (mm)	4.0	0.2
Number of gratings	1	4
Wavelength (nm)	1542	1521
Reflectivity (%)	> 50	< 0.1
Gauge length (mm)	4.0	FS 1 and FS 2: 10.0; FS 3: 35.0

Given the limitations of the analytical expression in (3), Finite element analysis (FE) of the membrane was undertaken to provide an understanding of the distribution of the strain over the membrane. The expected strain distribution over the working diameter of the membrane is

Optics EXPRESS

shown in Fig. 3, where it can be seen that the there is an annulus around the edge of the working area of the membrane that experiences compression, while the central region is in tension. The locations of the fibre segment interferometers and the FBG are also indicated in Fig. 3, showing that the FBG sensor, located at the centre of the membrane, would be expected to experience the maximum positive strain in response to positive pressurisation of the pressure chamber. FS 1 was also located over the region of the membrane that experienced positive strain, while FS 2 was positioned such that one half of its gauge length was bonded to the edge of the pressure responsive area of the membrane, where negative strains are predicted, with its other half attached to a section of membrane that was bonded to the aluminium support structure. FS 3 was not bonded to either the membrane or support structure, and thus experienced only the ambient temperature. It is clear from Fig. 3 that the FSI segments experience significant strain gradients, which would be expected to distort the spectrum of an FBG and thus compromise the ability to determine the average strain accurately [25]. Here, it is important to note that FSI integrates the strain induced phase shift over the length of the segment, and so the interrogation of the segment interferometer is not adversely affected by strain gradients.

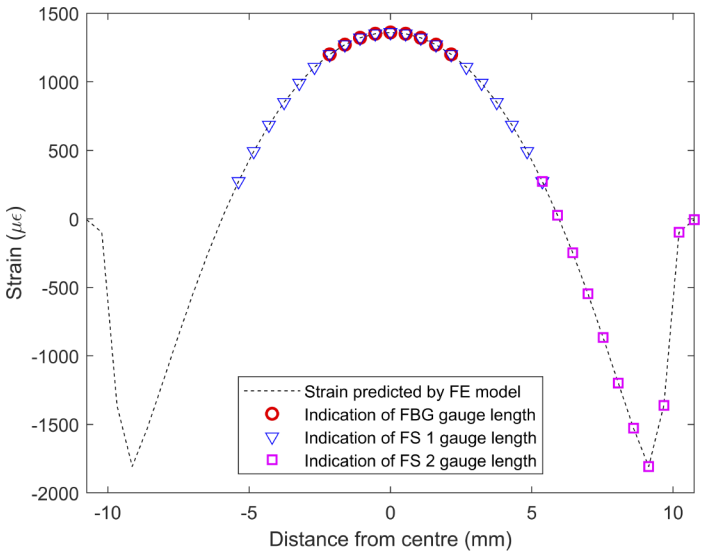

Fig. 3. Output from a Finite Element Analysis of the membrane under deflection with optical fibre mounted on the surface. Strain plotted at 35 kPa over the diameter of the membrane with the gauge lengths of the three sensors fibre optic sensors indicated by: red circles (◯) for the 4 mm long FBG, blue triangles (△) for the 10 mm long FS 1 and green squares (□) for the 5.75 mm long section of FS 2 bonded to the pressure responsive region of the membrane.

Figure 4 compares the predictions of the pressure induced strains experienced by the GFRP-mounted FBG and fibre segment interferometers using the elastic plate theory, based on Eq. (4), with that of the Finite Element Analysis. It is clear that the elastic plate theory predicts higher strains and that it cannot predict the compressive strain in the outer annulus.

2.2. Strain sensitivity

The strain sensitivity of an FBG results from the physical change in length of the optical fibre and the strain induced refractive index change, and has a value of 1.2 pm/$\mu\varepsilon$ for an FBG fabricated with a Bragg wavelength of 1550 nm in SMF 28 optical fibre [26]. The strain sensitivity of FSI

Optics EXPRESS

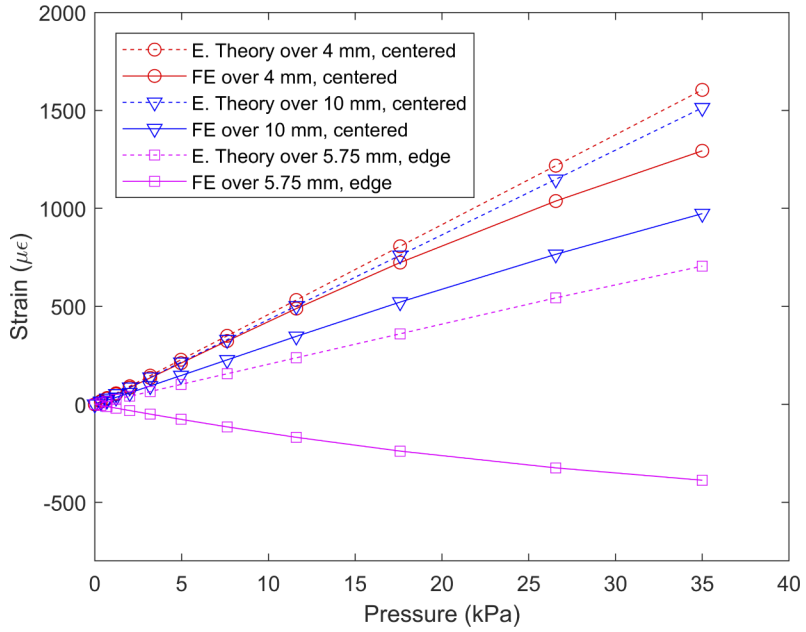

Fig. 4. Outputs from a Finite Element Analysis of the membrane under deflection and from the elastic plate theory based on Eq. (4). The strain is plotted over the pressure range of 0 to 35 kPa with the gauge lengths of the three sensors fibre optic sensors indicated by: red circles (◯) for the 4 mm long FBG, blue triangles (Δ) for the 10 mm long FS 1 and green squares (□) for the 5.75 mm long section of FS 2 bonded to the pressure responsive region of the membrane.

is determined [27] using Eq. (5) and is dependent on the gauge length, L.

$$\varepsilon = \frac{d\phi \cdot \lambda}{4L \cdot \pi \cdot n \cdot k} \tag{5}$$

where $d\phi$ is the strain induced phase change, n is the effective index of the propagating mode and λ is the wavelength of the interrogating laser. The strain gauge factor k is calculated from the strain-optic coefficient of the optic fibre [28], which has a value of 0.795 for SMF 28 optical fibre. The strain sensitivities of FBGs and FSI are provided in Table 3.

Table 3. Strain and predicted pressure sensitivities of the GFRP-mounted FBG and FSI sensor elements

	Strain Sensitivity	Predicted Pressure Sensitivity
FBG	1.2 pm/$\mu\varepsilon$	45.6 pm/kPa
FS 1	0.096 rad/$\mu\varepsilon$	2.77 rad/kPa
FS 2 (over 10 mm)	(0.096 rad/$\mu\varepsilon$)	/
FS 2 (over 5.75 mm)	0.055 rad/$\mu\varepsilon$	-1.21 rad/kPa
FS 3	0.335 rad/$\mu\varepsilon$	/

2.3. *Pressure sensitivity*

In order to establish the theoretical pressure sensitivities achievable using each of the optical fibre-based approaches for the proposed sensor, the output from the FE analysis was combined

Optics EXPRESS

with the strain sensitivities provided in Section 2.1 and Section 2.2. The FE results over the sections of the membrane corresponding to the locations of the FBG and FS 1 were averaged over 4 mm and 10 mm lengths to reflect the measurements that would be made by the sensors. Likewise, the FE predictions for the strains at the section at the edge of the membrane, corresponding to the location of FS 2, were averaged over a length of 5.75 mm, as illustrated in Fig. 3. The predicted strain sensitivities along with the corresponding pressure sensitivities are detailed in Table 3.

2.4. Thermal sensitivity

It is important to consider the thermal response of the sensor. The temperature sensitivity of FBGs is well-established, arising from a combination of the thermal expansion of the fibre and the thermally induced refractive index change and has a value of 10 pm/°C for an FBG written with a Bragg wavelength of around 1550 nm in SMF 28 optical fibre [29].

$$\frac{\Delta\lambda_{Bragg}}{\lambda_{Bragg}} = (\alpha + \xi)\Delta T \tag{6}$$

With α representing the thermal expansion coefficient of the optical fibre ($0.55 \times 10^{-6}/^{\circ}C$) and ξ the thermo-optic coefficient approximately equal to $10^{-5}/^{\circ}C$ for silica core fibres doped with germanium [30].

The temperature sensitivity of FSI is governed by the same glass properties as that of FBGs, but is dependent on the gauge length, L, and can be calculated [30] using Eq. (7). A factor of two is included as the light traverses the sensor gauge length twice in this configuration.

$$\frac{d\phi}{dT} = \frac{4\pi L}{\lambda}(n\alpha + \xi) \tag{7}$$

where δT is the temperature change while α represents the thermal expansion coefficient (CTE) of the optical fibre and ξ the thermo-optic coefficient, which have values of $0.55 \times 10^{-6}/^{\circ}C$ and $10^{-5}/^{\circ}C$ for silica core fibres doped with germanium, respectively [30]. Assuming a value of 1.456 for the refractive index, n, at an operating wavelength λ =1521 nm [26], we obtain:

$$\frac{d\phi}{dT} = L \cdot 89 \;\; rad/m^{\circ}C \tag{8}$$

2.5. Experimental configuration

2.5.1. Pressure response characterisation

Figure 5 illustrates the experimental configuration used to characterise the pressure sensor. The FBG was interrogated using a commercially available FBG interrogator (SmartScan - SmartFibres UK) specified to provide a 1 pm resolution for Bragg wavelength changes, operating with a data rate of 250 Hz. The FSI sensors were interrogated using an in-house designed and built RRI interrogator [23] operating at a bandwidth of 1 kHz. A Texance PDif pressure sensor provided a reference measurement, logging at a rate of 250 Hz. The pressure was delivered to both the optical sensor chamber (Fig. 1) and to the reference sensor by a pressure controller (Pace 6000) over a range of ±35 kPa with accuracy of ±0.02% of the full scale. The experiment was performed in a stable thermal environment, maintained at 22°C±0.5°C.

2.5.2. Thermal characterisation

Figure 6 illustrates the experimental configuration used to characterise the thermal response of the sensor. The two optical fibre sensor interrogators detailed in Section 2.5.1 were used. The pressure sensor was placed in a Vötsch VTM 7004 oven and two thermocouples recorded the temperature on the surface of the aluminium support. The thermocouples were terminated with polyimide thin film and were secured to the support structure using polyimide tape. The temperature of the oven was varied from 37 °C to 82 °C.

Optics EXPRESS

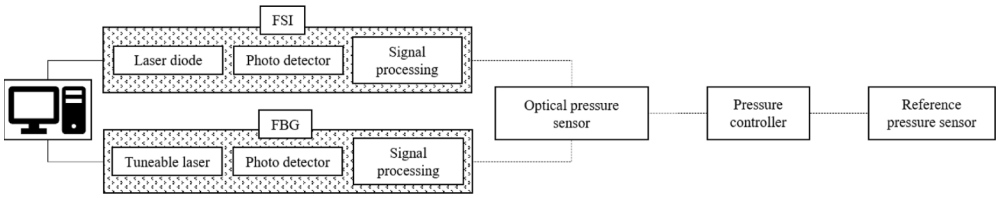

Fig. 5. Schematic diagram of experimental configuration used to characterise the pressure sensor

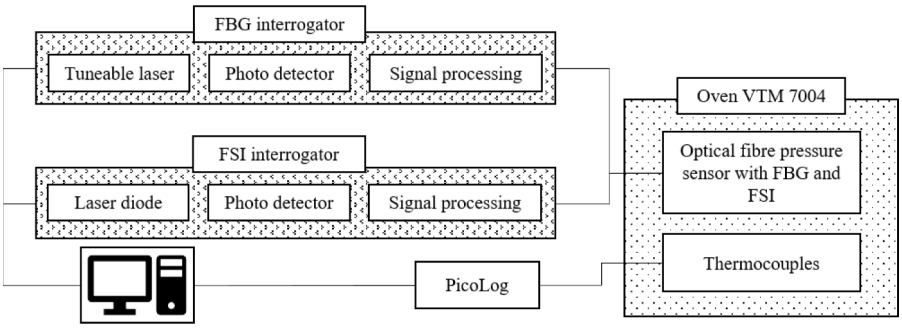

Fig. 6. Schematic diagram of the experiment set up used to characterise the thermal response of the system

3. Results and discussions

3.1. Pressure sensor characterisation

To facilitate the comparison of the performances of the FBG and the FSI sensors, and to correlate their responses with the output from the FE model, their responses have been converted to strain. The data obtained from a series of pressure cycles are shown in Fig. 7. The pressure measurement provided by the Texance PDif pressure sensor is shown on the right-hand y-axis, while the strains measured by each of the fibre sensor elements are shown on the left-hand y-axis. As described previously, FS 3 does not experience any strain, as this segment is not bonded to the membrane. FS 2 exhibits negative strain and FS 1 positive strain, matching the output from the FE model shown in Fig. 3 with the FBG sensor exhibiting more strain than FS 1.

The calibration curves presented in Fig. 8 show the pressure sensitivities of the optical fibre sensors. The wavelength shift exhibited by the FBG sensor at each pressure step is plotted against applied pressure on the right-hand y-axis, while the phase changes of FS 1 and FS 2 are plotted on the left-hand y-axis. The optical fibre sensors show linear responses. The FBG based sensor exhibits a sensitivity of 95±7.6 pm/kPa, while FS 1 and FS 2 exhibit 6.3±0.43 rad/kPa and -2.6±0.32 rad/kPa respectively.

Qualitatively, the form of the data obtained from each of the optical fibre sensors are in agreement with the FE output. The converted strain-pressure responses indicate that FS 1 experienced a lower strain than that experienced by the FBG, due to the integration of the strain over a gauge length that has a large strain gradient, and the response of FS 2 is of opposite sign, as expected from the compressive strain at the edge of the membrane predicted by the FEA results shown in Fig. 3 and Fig. 4. FS 3 does not respond to pressure as the segment is not mounted on the membrane. By combining Eq. (4) with the measured sensitivities, it can be shown that the center cores of the FBG and FSI optical fibres are located about 380 μm and 310 μm above the surface of the membrane respectively, which suggests that the glue line has a thickness of about 250 μm, taking into account the 250 μm coating diameter of the FBG fibre and the 125

Optics EXPRESS

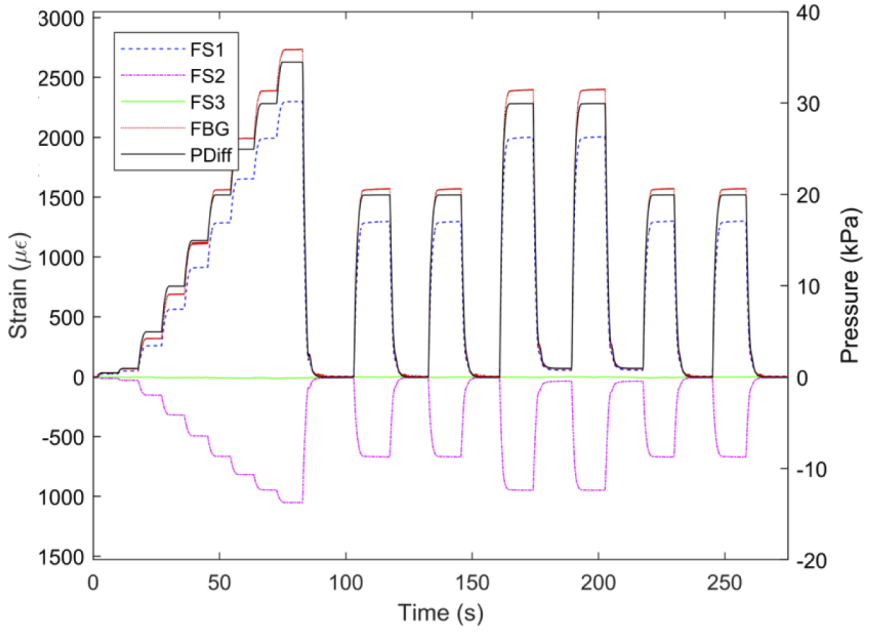

Fig. 7. Measurements obtained from the optical fibre sensors and the electrical pressure sensor (Texance, PDiff) during a series of pressure cycles. The optical fibre sensor responses are plotted in terms of the strain, facilitating comparison of the sensor responses. Left-hand axis: strain measured by optical fibre sensors. Right-hand axis: output from the electrical pressure sensor.

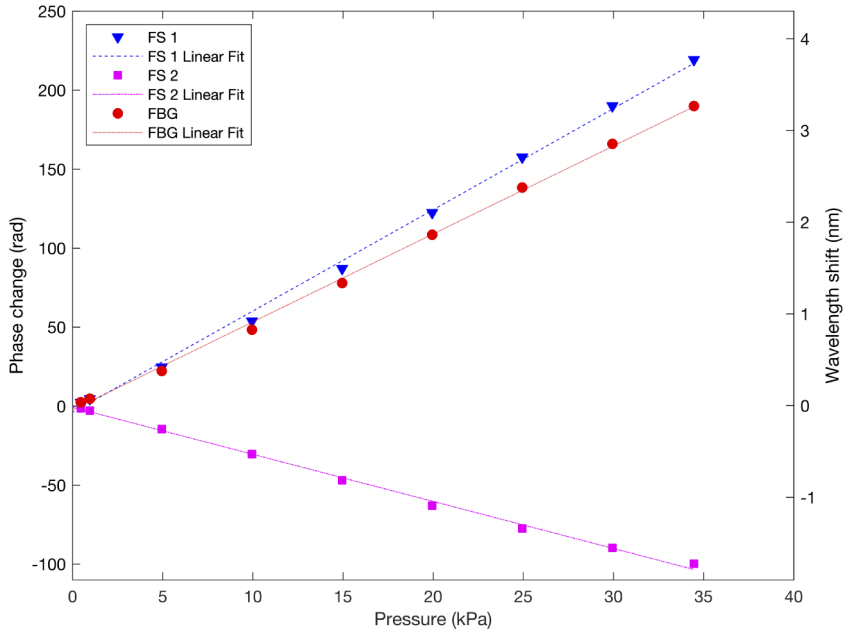

Fig. 8. Pressure phase change and wavelength shift of FSI segments and FBG sensor with linear fits. Left-hand axis: Blue triangle (Δ) represents FS 1 with a linear fit $R^2 = 0.9972$ and pink square (□) represents FS 2 with a linear fit $R^2 = 0.9973$. Right-hand axis: Red circle (◯) represents the FBG with a linear fit $R^2 = 0.9981$. The linear coefficients are reported in the Table 6.

Optics EXPRESS

μm cladding diameter of the FSI fibre as the coating was removed over the whole section from first to last grating. This is consistent with measurements made from cross sections of similar fibre-bonded membranes.

3.2. Thermal characterisation

Figure 9 shows the responses of the thermocouple and FBG sensor in Fig. 9 (a) and the three FSI sensors in Fig. 9 (b) as the temperature was increased in steps. The data shown in Fig. 9 (a) was used to produce a temperature calibration for the FBG based pressure sensor, shown in Fig. 10. The data shown in Fig. 9 (b) was used for FS 1, FS 2 and, FS 3. Figure 9 (b) highlights the lower response of FS 2 at the edge of the membrane, as well as the close relationship of the thermal responses of FS 1 and FS 3, even though FS 1 is fully bonded to the membrane and 3.5 times shorter than the unbonded FS 3. FS 1 appears to have a slight thermal lag in comparison with the free segment, which can be explained by the thermal inertia of the bonded GFRP membrane and aluminium support.

The calibration curves in Fig. 10 show the temperature sensitivities of each optical sensor, determined by correlating the optical measurements with those from the thermocouples, using the data presented in Fig. 9. The FBG wavelength shift (◯) is shown on the right-hand y-axis and the FS phase changes are shown on the left-hand y-axis. It is clear that the sensitivities of both FS 1 (△) and FS 3 (⋄) are similar and that FS 2 (□) is lower. All sensors exhibit linear responses. The FBG exhibits a sensitivity of 43±1 pm/°C, while the sensitivities of the other gauges were recorded as; FS 1 3.6±0.15 rad/°C, FS 2 2.5±0.15 rad/°C and FS 3 3.7±0.15 rad/°C.

The temperature sensitivities of FS 1, FS 2 and the FBG are influenced by the thermal expansion of the sensor structure as they are bonded to the GFRP membrane, which, in turn, is also mounted on the aluminium support. Equation (6) shows that the thermal sensitivity of free optical fibres is dominated by the thermo-optically-induced refractive index change, with the thermal expansion component being a factor of 10 smaller. However, in the sensor configuration described here, the thermal expansion is also influenced by the membrane and the support structure assembly. The challenge here is that while the thermal expansion coefficient of aluminium is well known to be 23 x 10^{-6}/°C, the CTE of GFRP depends on many factors, such as fibre resin ratio, fibre orientation, void volume, and can vary from 1 to 20 x 10^{-6}/°C [31–33].

In order to understand issues concerning the design of the sensor, additional experiments were performed to investigate the influence of material selection on the thermal response. The investigation involved the comparison of the thermal responses of an unmounted, free, FBG with those of FBGs bonded to an unsupported membrane and to a membrane that was mounted in the aluminium support. The data are shown in Fig. 11. In each case, an FBG encapsulated in a fused silica capillary was used for temperature sensing only. The unmounted FBG and the encapsulated FBG exhibit similar sensitivities of 11 pm/°C. The GFRP-bonded FBG shows a sensitivity of 16 pm/°C, which increased to 43 pm/°C when the membrane is bonded to the aluminium support. This correlates with the sensitivity determined in Section 3.2.

By replacing the optical fibre's CTE with that of aluminium in Eq. (6), the theoretical values are seen to be in alignment with the experimental results and are presented in Table 4. The experimentally determined thermal sensitivity of the optical fibre bonded to the GFRP membrane suggests that the CTE of the membrane is in the order of 5 x 10^{-6}/°C. In this configuration, the thermal properties of the aluminium appear to dominate over those associated with the membrane or adhesive.

The thermal sensitivities of FS 1 and FS 2 can be calculated using the parameters shown in Table 4. By using the value of α for aluminium in Eq. (7), we obtain a sensitivity of 3.6 rad/°C, which correlates well with the experimental measurement of FS 1. The predicted and measured values for all FSI are summarised in Table 5. FS 2 exhibits a lower temperature dependence, which can be explained by considering the mounting of the fibre segment, which is partly bonded

Optics EXPRESS

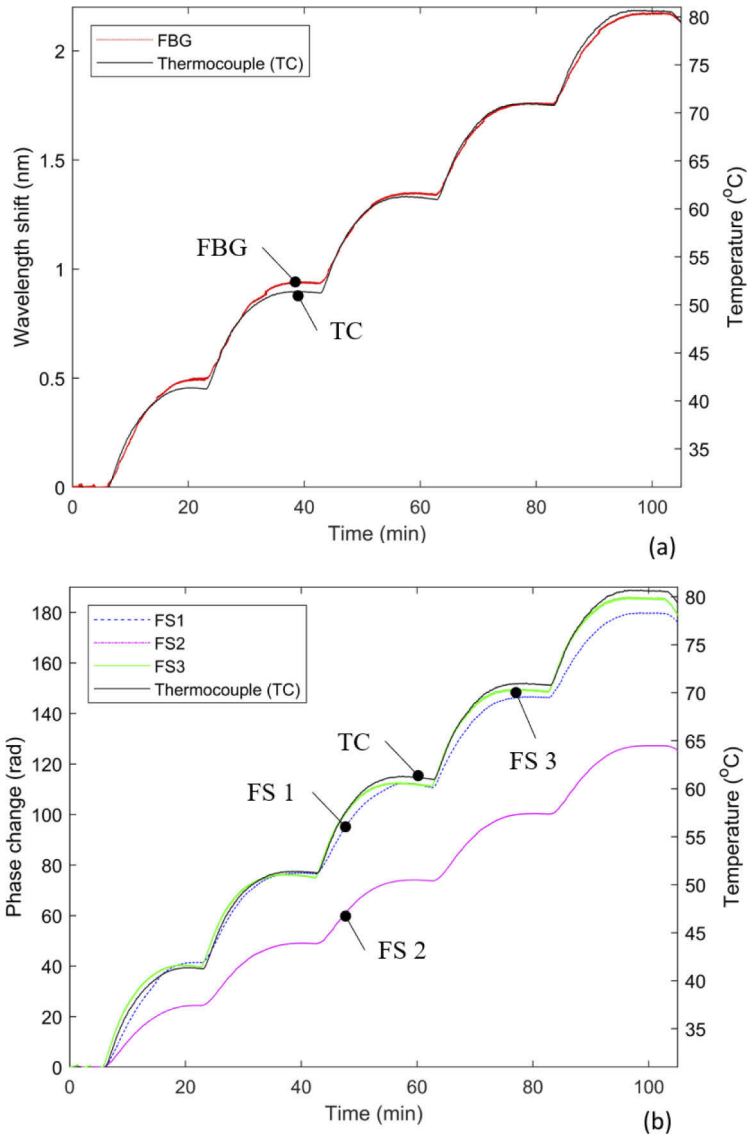

Fig. 9. Optical fibre sensors and thermocouple raw responses plotted as a function of time. (a) FBG and thermocouple and (b) FS 1, FS 2, FS 3 and thermocouple.

Table 4. FBG thermal sensitivities for bare and specimen-mounted fibre.

	α ($\mu\varepsilon$/°C)	Theoretical (pm/°C)	Experimental (pm/°C)
SMF 28 Optical Fibre	0.55	11	11
GFRP Membrane	1 to 20	10 to 40	16
Aluminum Pressure Chamber	23	46	43

Optics EXPRESS

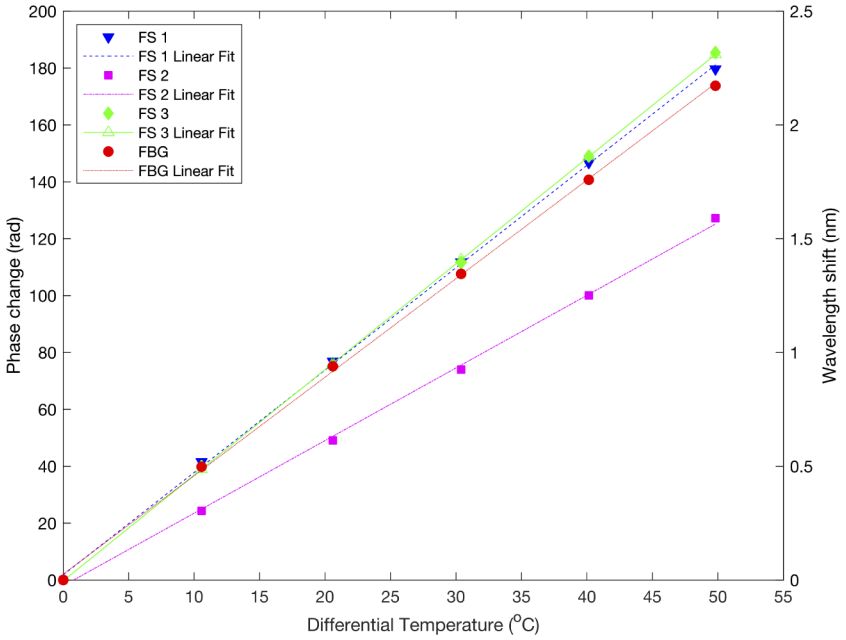

Fig. 10. Thermal phase change and wavelength shift of FSI segments and FBG sensor with linear fits. Left-hand axis: Blue triangle (△) represents FS 1 with a linear fit $R^2 = 0.9992$, pink square (□) represents FS 2 with a linear fit $R^2 = 0.9969$ and green lozenge (⋄) represents the FS 3 with a linear fit $R^2 = 0.9999$. Right-hand axis: Red circle (◯) represents the FBG with a linear fit $R^2 = 0.9992$.

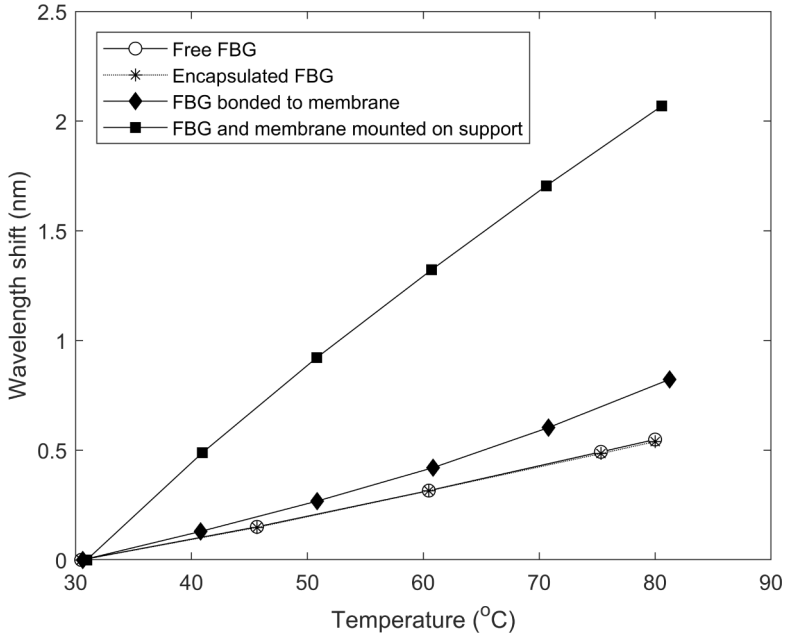

Fig. 11. Thermal response of a free FBG, an encapsulated FBG, an FBG bonded to an unsupported GFRP membrane and an FBG and membrane mounted to the aluminium support. Note that the data points for the free and encapsulated FBGs are coincident in this graph.

Optics EXPRESS

to the free-standing part of the membrane and partly to the section of membrane that is bonded to the aluminium support. Thus, a 5.8 mm long portion on the right hand side of FS 2 in Fig. 1 is in similar condition to that of FS 1, so that it can be assumed that this portion experiences the thermal expansion of the aluminium support, giving a thermal sensitivity of 2.1 rad/°C. The 4.3 mm long section on the right hand side of FS 2 is influenced by both the GFRP and aluminium, which counteract each other's thermal expansion. The thermal sensitivity of the part of this segment is thus calculated to be 0.77 rad/°C. A total sensitivity of 2.8 rad/°C is then predicted for FS 2, assuming that the reflectors forming FS 1 are equally spaced about the centre of the membrane. This differs from the experimentally determined value by 12%, which can be explained by the uncertainty of the exact position of the segment on the membrane. The experimentally measured sensitivity of FS 2 suggests that the segment is bounded to a 4 mm long free centre section of the membrane rather than the expected 5.8 mm, which may reflect the accuracy with which the absolute locations of the FSI reflectors within the fibre were known.

Table 5. Predicted and measured FSI thermal sensitivities

	FS 1	FS 2	FS 3
Predicted (rad/°C)	3.6	2.8	3.2
Measured (rad/°C)	3.6	2.5	3.7

3.3. *Pressure - temperature cross-sensitivity*

The coefficients for the pressure and temperature responses of the membrane-bonded FSI and FBG sensors when the membrane is mounted in the aluminium support structure, determined experimentally in sections 3.1 and 3.2, are summarised in Table 6.

Table 6. Optical fibre sensor pressure and temperature linear coefficients determined from the experimental data.

	Pressure Coefficient K_P	Temperature Coefficient K_T
FBG	95±4.4 pm/kPa	43±1 pm/°C
FS 1	6.3±0.2 rad/kPa	3.6±0.1 rad/°C
FS 2	-2.6±0.3 rad/kPa	2.5±0.1 rad/°C
FS 3	/	3.7±0.1 rad/°C

The existence of regions on the diaphragm that show similar thermal sensitivities but pressure sensitivities of opposite sign suggests the potential for the discrimination of the temperature and pressure responses of the sensor by solving a pair of linear equations using a matrix operation. In general, when considering the performance of sensors capable of discriminating between the influences of two measurands, an analysis of the conditioning of the matrix of coefficients is undertaken, with the condition number providing an indicator of the sensitivity of the solutions to errors in the data [34]. This may be followed by an analysis of the error propagation and an estimate of the uncertainties in the calculated values of the measurands [35]. The temperature and pressure discrimination can also be achieved by decoupling their frequencies [36]. For optical fibre based pressure sensors, in many published cases it is, however, assumed that there is no cross sensitivity or experiments to validate the theoretical performance and the matrix operation performance are not presented.

The sensor shown in Fig. 1 was placed in the oven and pressure applied using the experimental set up shown in Fig. 5. While the temperature varied from ambient to up to 82 °C, the pressure was applied according to the cycles shown in Fig. 7. The temperature of the oven was stabilised at 37°C, 62°C and 82°C. The results of changing the pressure in the chamber in step-wise fashion are shown in Fig. 12.

Optics EXPRESS

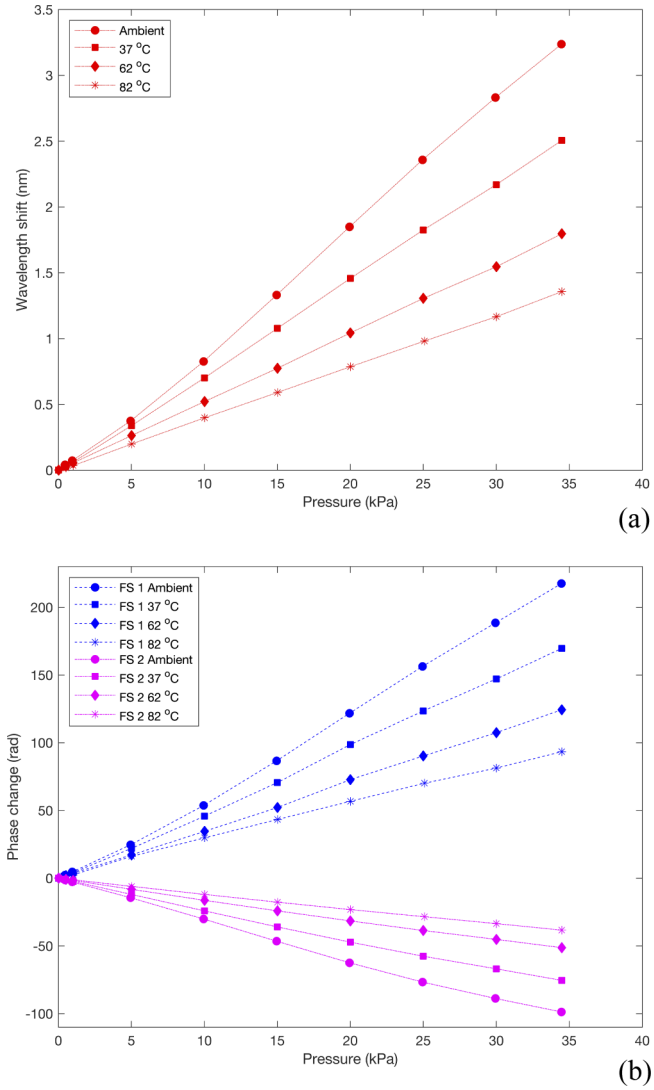

Fig. 12. Pressure responses at ambient (◯) 37°C (□), 62°C (⋄) and 82°C (∗) for (a) the FBG sensor and (b) the FS 1 sensor in blue (positive phase change) and FS 2 sensor in pink (negative phase change).

Optics EXPRESS

It can be seen that the temperature greatly influences the pressure response of the sensor, showing a decrease in sensitivity when temperature increases. The pressure sensitivity at each temperature is detailed in Table 7. As seen in Fig. 11 and Table 4, the thermal expansion of the aluminium support acts to mechanically load the membrane, which stiffens the sensor and reduces the deformation of the membrane in response to pressure changes.

Table 7. Pressure sensitivities measured at different temperatures

	Ambient	37°C	62°C	82°C
FBG (pm/kPa)	95±4.4	73±3.3	52±1.6	39 ±2.3
FS 1 (rad/kPa)	6.3±0.2	4.9±0.2	3.6±0.2	2.7±0.2
FS 2 (rad/kPa)	-2.6±0.3	-2.3±0.3	-1.5±0.3	-1.1±0.3

The influence of temperature on the pressure response is illustrated clearly by comparing the strains experienced by the optical fibre sensors during step-wise changes in pressure, carried out at two constant temperatures, ambient and 80°, as shown in Fig. 13.

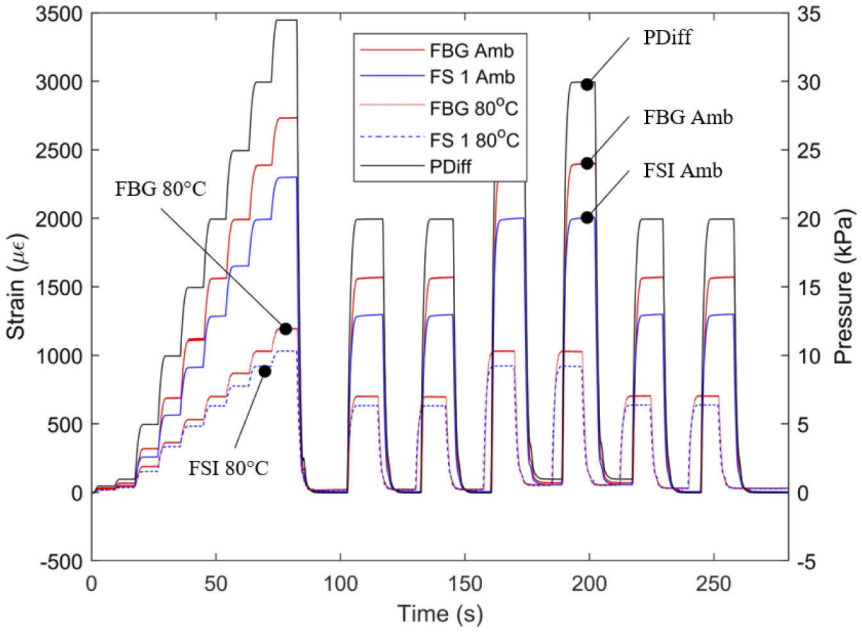

Fig. 13. Left axis: Comparison of FS 1 and FBG sensors at ambient and 80°C with applied pressure showing the reduced pressure sensitivity at elevated temperature. Right axis: PDiff reference electronic pressure sensor. Note that the timing of the pressure steps in the two experiments differed slightly, which is the cause of the apparent offset between the time series.

Furthermore, it has been observed that changes in temperature during a measurement will change the base line in a non-linear fashion, compromising significantly the measurement even when an independent measurement of temperature is provided by a thermocouple, and the cross sensitivity means that it would not be possible to ignore the influence of temperature even in dynamic measurements, where the temperature varies on a different timescale to the pressure. The use of higher order compensation techniques to take into account the cross sensitivity to measurands was reported in [37], where a Taylor expansion was used to generate simultaneous equations taking into account the cross sensitivity. This approach is inappropriate for use here due to the large pressure and temperature excursions and the non linearity of the cross sensitivity.

Optics EXPRESS

The results highlight the importance of the selection of the material used to package the sensor, especially when the sensor is to operate in an environment subject to temperature variations. While this is not a new observation, the analysis shown here identifies the origin of the effects and highlights the importance of undertaking a full experimental study of cross sensitivity issues when designing optical fiber based sensors. In the design of electrical pressure sensors where the pressure induced deformation of diaphragm is monitored using piezo-resistive sensors, matching the thermal expansion of the support structure and the diaphragm is noted to be a means for minimising thermo-mechanical influences on the pressure response [38,39]. It is informative to consider a sensor of the type shown in Fig. 1, in which the support structure should be thermally balanced with the membrane, thus removing the thermal cross-sensitivity. A housing with a CTE value of 5 x 10^{-6}/°C would greatly alleviate the errors, although other factors such as specific heat capacity will also have an influence in dynamic thermal environments. For this hypothetical sensor, the thermal responses of fibre segments FS 1 and FS 2 can be recalculated using the CTE of the GFRP reported in Section 3.2 at 5 x 10^{-6}/°C. The sensor's response can then be expressed in a matrix that has the coefficients indicated in Table 8, with matrix inversion used to discriminate the two parameters.

Table 8. FS 1 and FS 2 pressure and temperature coefficients determined for a hypothetical sensor, where the support structure is made from the same material as the diaphragm to avoid a thermal dependence of the pressure sensitivity

	Pressure Coefficient K_P	Temperature Coefficient K_T
FS 1	6.3 rad/kPa	1.8 rad/°C
FS 2	-2.6 rad/kPa	1.8 rad/°C

The condition number of the matrix for this hypothetical sensor is 3.0, suggesting the matrix to be well-conditioned with the error in the measurements not impacting significantly the discrimination of the two parameters. The validation of this is the subject of on-going work.

3.4. Performance comparison

The general noise behaviours of the FBG, FS 1 and the electrical pressure sensor are compared in Fig. 14. At a bandwidth of 250 Hz, the FBG sensor exhibits noise with a standard deviation of 0.75 $\mu\varepsilon$, while FSI segment FS 1 achieves a noise standard deviation of 0.04 $\mu\varepsilon$ over a much higher bandwidth of 1 kHz. When converted to pressure using the respective calibration curves from Fig. 8, the standard deviations correspond to 9.5 Pa for the FBG and 0.61 Pa for FS 1, where the FS 1 sensor exceeds the pressure resolution of the electrical pressure sensor, which has a noise standard deviation of 1.3 Pa at 250 Hz bandwidth. These values are summarised in Table 9. During the recording time of Fig. 14, the pressure was maintained at 0 Pa, followed by the a ramp to 500 Pa. The response to the start of the increase in pressure can be located on the later part of the time series, at approximately 0.42 s. It can be seen that only FS 1 is able to resolve the pressure wave at 80 Hz that is a result of the pumping action of the pressurisation system. Even though the FSI sensor has the higher inherent strain response due to the longer gauge length used, these results confirm that the much higher resolution of the FSI interrogation approach results in an overall increase in the pressure sensitivity of the system by more than 15 times.

Table 9. Comparison of the noise performance of the investigated sensing technologies

	FBG	FSI	Electrical
Bandwidth	250 Hz	1 kHz	250 Hz
Noise (strain)	0.75 $\mu\varepsilon$	0.04 $\mu\varepsilon$	-
Noise (pressure)	9.5 Pa	0.61 Pa	1.3 Pa

Optics EXPRESS

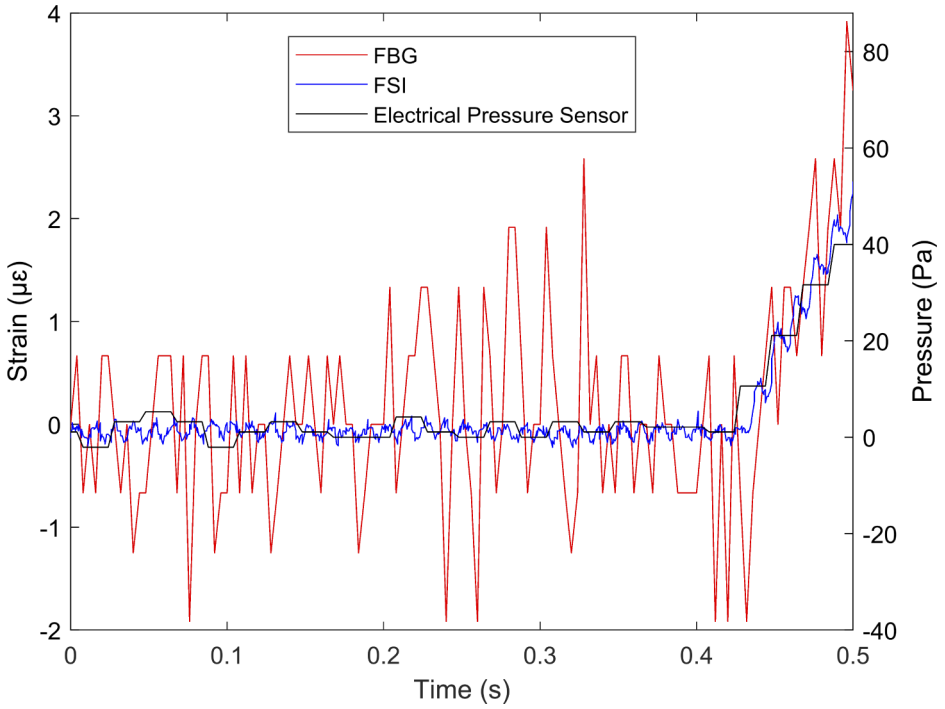

Fig. 14. Change in pressure showing the fast response of each sensor. The wave behavior appearing in in the FS 1 sensor data can be directly traced back to the pressure pump use. Here, the same dataset as used in Fig. 7 was used.

The fundamental measurement principles of both FSI and FBGs are based on changes in the same physical glass properties of optical fibres [28] in response to strain and temperature. Therefore, for similar physical placement of the sensing element on the diaphragm, the repeatability of the measurement will depend solely on the performance of the interrogators, which for FBG interrogators will have been documented by the interrogation system manufacturers and for FSI has been discussed elsewhere [22,23]. Furthermore, as can be seen in Fig. 3, the existence of strong strain gradients [25] across the diaphragm makes the exact placement of the sensing element on the diaphragm important, potentially affecting reproducibility. Here, for FBGs, the effect of strain gradients can potentially lead to distorted readings between different sensors, depending on the exact location of the FBG and on the peak finding algorithm used within the interrogator. However, for FSI, where the interferometric measurement principle guarantees an exact integration of the strain within the sensing region, strain gradients are not expected to significantly influence on the fidelity of the measurement, therefore making the exact placement of the sensing region less critical.

4. Conclusions

The performance of a pressure sensor that relies upon the optical fibre based measurement of the strain induced by the deflection of a GFRP membrane has been investigated. Two approaches to the measurement of strain have been compared; the well-established FBG approach and the new interferometric technique. At ambient temperature, the reported pressure sensitivity achieved using an FBG bonded to the centre of the membrane was 95±7.6 pm/kPa with the corresponding sensitivity of an FSI segment, with its the reflectors spaced approximately equally about the centre of the membrane, being 6.3±0.43 rad/kPa. Taking into consideration the noise behaviour

Optics EXPRESS

of the two interrogation approaches, their pressure resolutions exceed the design specification target of 23 Pa, with values of 9.5 Pa and 0.61 Pa, respectively. Exploiting the characteristics of the membrane revealed in an FE study, where an annulus of compressive strain is revealed near the outer circumference of the free area of the membrane, a fibre segment interferometer was arranged to measure the positive strain over the central region of the membrane, and another to measure the compression at the edge. With increasing temperature, the measured pressure sensitivities were observed to decrease due to the high CTE of the aluminium support, which acted to tension the membrane, increasing its stiffness. This shows the importance of the material selection for all parts of the assembly. It is suggested that the response of these FSI segments can be used for the separation of the temperature and pressure responses of the membrane with very low errors when used with the same material throughout. Further work involves consideration of the material characteristics of the support/pressure chamber to validate the temperature/pressure discrimination.

Funding. Royal Academy of Engineering UK (RF/201718/1745); Engineering and Physical Sciences Research Council UK (EP/N002520/1).

Disclosures. The authors declare no conflicts of interest.

Data availability. The underlying data can be accessed from the Cranfield Online Research Data Repository at http://dx.doi.org/10.17862/cranfield.rd.13118306.

References

1. J. C. van der Linden and H. A. Mensink, "Linear and angular position measurement of aircraft components," AGARD Flight Test Instrumentation Series 8, (1977).
2. T. L. Grigorie and R. M. Botez, *Control techniques for a smart actuated morphing wing model: Design, numerical simulation and experimental validation* (Butterworth-Heinemann, 2018351–397, Morphing Wing Technologies: Large Commercial Aircraft and Civil Helicopters
3. R. W. Ainsworth, R. J. Miller, R. W. Moss, and S. J. Thorpe, "Unsteady pressure measurement," Meas. Sci. Technol. **11**(7), 1055–1076 (2000).
4. E. Kottkamp, H. Wilhelm, and D. Kohl, "Strain gauge measurements on aircraft," AGARDograph, (1976).
5. F. Trenkle and M. Reinhardt, "In-flight temperature measurements," AGARD Flight Test Instrumentation Series 2, (1973).
6. P. C. Berri, M. D. L. Dalla Vedova, P. Maggiore, and T. Scolpito, "Feasibility study of fbg-based sensors for prognostics in aerospace applications," in *Journal of Physics: Conference Series*, vol. 1249 (2019).
7. C. E. Campanella, A. Cuccovillo, C. Campanella, A. Yurt, and V. M. N. Passaro, "Fibre Bragg grating based strain sensors: Review of technology and applications," Sensors **18**(9), 3115–00 (2018).
8. T. Kissinger, E. Chehura, S. E. Staines, S. W. James, and R. P. Tatam, "Dynamic fiber-optic shape sensing using fiber segment interferometry," J. Lightwave Technol. **36**(4), 917–925 (2018).
9. M. G. Xu, L. Reekie, Y. T. Chow, and J. P. Dakin, "Optical in-fibre grating high pressure sensor," Electron. Lett. **29**(4), 398–399 (1993).
10. R. Correia, E. Chehura, S. W. James, and R. P. Tatam, "A pressure sensor based upon the transverse loading of a sub-section of an optical fibre Bragg grating," Meas. Sci. Technol. **18**(10), 3103–3110 (2007).
11. Y. Zhang, D. Feng, Z. Liu, Z. Guo, X. Dong, K. S. Chiang, and B. C. B. Chu, "High-sensitivity pressure sensor using a shielded polymer-coated fiber Bragg grating," IEEE Photonics Technol. Lett. **13**(6), 618–619 (2001).
12. R. R. J. Maier, J. S. Barton, J. D. C. Jones, S. McCulloch, and G. Burnell, "Dual-fibre Bragg grating sensor for barometric pressure measurement," Meas. Sci. Technol. **14**(11), 2015–2020 (2003).
13. M. G. Xu, H. Geiger, and J. P. Dakin, "Fibre grating pressure sensor with enhanced sensitivity using a glass-bubble housing," Electron. Lett. **32**(2), 128–129 (1996).
14. T. Yamate, R. T. Ramos, R. J. Schroeder, R. Madhavan, S. C. Balkunas, and E. Udd, "Transversely loaded Bragg grating pressure transducer with mechanically enhancing the sensitivity," in *2002 15th Optical Fiber Sensors Conference Technical Digest, OFS 2002* (2002), pp. 535–538.
15. L. Liu, Y. Li, Y. He, F. Li, and Y. Liu, "Membrane-based fiber Bragg grating pressure sensor with high sensitivity," Microw. Opt. Technol. Lett. **51**(5), 1279–1281 (2009).
16. W. T. Zhang, F. Li, Y. L. Liu, and L. H. Liu, "Ultrathin FBG pressure sensor with enhanced responsivity," IEEE Photonics Technol. Lett. **19**(19), 1553–1555 (2007).
17. A. G. Leal-Junior, A. Frizera, and C. Marques, "Thermal and mechanical analyses of fiber Bragg gratings-embedded polymer diaphragms," IEEE Photonics Technol. Lett. **32**(11), 623–626 (2020).
18. J. Huang, Z. Zhou, X. Wen, and D. Zhang, "A diaphragm-type fiber Bragg grating pressure sensor with temperature compensation," Measurement **46**(3), 1041–1046 (2013).
19. Z. Jia, Q. Fan, D. Feng, D. Yu, X. Zhao, and K. Yang, "Design and investigation of the fiber Bragg grating pressure sensor based on square diaphragm and truss-beam structure," Opt. Eng. **58**(09), 1 (2019).

Optics EXPRESS

20. D. Song, J. Zou, Z. Wei, Z. Chen, and H. Cui, "Liquid-level sensor using a fiber Bragg grating and carbon fiber composite diaphragm," Opt. Eng. **50**(1), 014401 (2011).
21. L. F. Aime, A. Verzeletti, S. W. James, and R. P. Tatam, "Optical fiber Bragg grating based pressure sensor using a composite diaphragm for pressure measurements," in *2019 IEEE Sensors Conference, Montreal* (2019).
22. T. Kissinger, R. Correia, T. O. H. Charrett, S. W. James, and R. P. Tatam, "Fiber segment interferometry for dynamic strain measurements," J. Lightwave Technol. **34**(19), 4620–4626 (2016).
23. T. Kissinger, T. O. H. Charrett, and R. P. Tatam, "Range-resolved interferometric signal processing using sinusoidal optical frequency modulation," Opt. Express **23**(7), 9415–9431 (2015).
24. J. N. Reddy, *Theory and Analysis of Elastic Plates and Shells*, 2nd Edition (CRC, 2006).
25. A. Rajabzadeh, R. Heusdens, R. C. Hendriks, and R. M. Groves, "Calculation of the mean strain of smooth non-uniform strain fields using conventional FBG sensors," J. Lightwave Technol. **36**(17), 3716–3725 (2018).
26. Y.-J. Rao, "In-fibre Bragg grating sensors," Meas. Sci. Technol. **8**(4), 355–375 (1997).
27. T. Kissinger, T. O. H. Charrett, and R. P. Tatam, "Fibre segment interferometry using code-division multiplexed optical signal processing for strain sensing applications," Meas. Sci. Technol. **24**(9), 094011 (2013).
28. J. Roths and F. Julich, "Determination of strain sensitivity of free fiber Bragg gratings," Proc. SPIE **7003**, 700308 (2008).
29. K. O. Hill and G. Meltz, "Fiber Bragg grating technology fundamentals and overview," J. Lightwave Technol. **15**(8), 1263–1276 (1997).
30. G. B. Hocker, "Fiber-optic sensing of pressure and temperature," Appl. Opt. **18**(9), 1445–1448 (1979).
31. R. R. Johnson, M. H. Kural, and G. B. Mackey, "Thermal expansion properties of composite materials," NASA Contractor Report 165632 (1981).
32. M. A. Pop, D. Motoc, A. Constantinescu, V. Geaman, and R. Derczeni, "Cte assessment of various glass fibre reinforced polymer composite architectures," Metalurgia International **18**, 131–134 (2013).
33. J. G. Mohr and S. o. t. P. Industry, *SPI Handbook of Technology and Engineering of Reinforced Plastics/composites* (Van Nostrand Reinhold Company, 1973).
34. W. Jin, W. C. Michie, G. Thursby, M. Konstantaki, and B. Culshaw, "Geometric representation of errors in measurements of strain and temperature," Opt. Eng. **36**(8), 2272–2278 (1997).
35. W. Jin, W. C. Michie, G. Thursby, M. Konstantaki, and B. Culshaw, "Simultaneous measurement of strain and temperature: error analysis," Opt. Eng. **36**(2), 598–609 (1997).
36. A. G. Leal-Junior, A. Daaz Camilo, A. R.and Frizera, C. Marques, M. R. N. Ribeiro, and M. J. Pontes, "Simultaneous measurement of pressure and temperature with a single fbg embedded in a polymer diaphragm," Opt. Laser Technol. **112**, 77–84 (2019).
37. F. Farahi, D. J. Webb, Jones, J. D. C. , and Jackson, "Simultaneous measurement of temperature and strain: cross-sensitivity considerations," J. Lightwave Technol. **8**(2), 138–142 (1990).
38. Q. Yu and X. Zhou, "Pressure sensor based on the fiber-optic extrinsic Fabry-Perot interferometer," Photonic Sens. **1**(1), 72–83 (2011).
39. Kulite sensing technology, https://kulite.com//assets/media/2018/01/section2.pdf. Accessed: 2020-08-17.

2021-01-25

High sensitivity pressure measurement using optical fibre sensors mounted on a composite diaphragm

Aime, Laura F. J.

Optical Society of America

Aime LFJ, Kissinger T, James SW, et al., (2021) High sensitivity pressure measurement using optical fibre sensors mounted on a composite diaphragm. Optics Express, Volume 29, Issue 3, 2021, pp. 4105-4123

https://doi.org/10.1364/OE.416715